Mott and generalized Wigner crystal states in WSe_2/WS_2 moiré superlattices

Emma C. Regan[1,2,3]†, Danqing Wang[1,2,3]†, Chenhao Jin[1,4]†, M. Iqbal Bakti Utama[1,3,5], Beini Gao[1,6], Xin Wei[1,7], Sihan Zhao[1], Wenyu Zhao[1], Zuocheng Zhang[1], Kentaro Yumigeta[8], Mark Blei[8], Johan Carlstroem[1,9], Kenji Watanabe[10], Takashi Taniguchi[10], Sefaattin Tongay[8], Michael Crommie[1,3,11], Alex Zettl[1,3,11], Feng Wang[1,3,11*]

[1] Department of Physics, University of California at Berkeley, Berkeley, California 94720, United States.

[2] Graduate Group in Applied Science and Technology, University of California at Berkeley, Berkeley, California 94720, United States.

[3] Material Science Division, Lawrence Berkeley National Laboratory, Berkeley, California 94720, United States.

[4] Kavli Institute at Cornell for Nanoscale Science, Ithaca, NY 14853, United States.

[5] Department of Materials Science and Engineering, University of California at Berkeley, Berkeley, California 94720, United States.

[6] Department of Physics, Huazhong University of Science and Technology, Wuhan 430074, China.

[7] School of Physics, University of Chinese Academy of Sciences, Beijing 100049, China.

[8] School for Engineering of Matter, Transport and Energy, Arizona State University, Tempe, Arizona 85287, United States.

[9] Department of Physics, Lund University, 221 00 Lund, Sweden.

[10] National Institute for Materials Science, 1-1 Namiki, Tsukuba, 305-0044, Japan.

[11] Kavli Energy NanoSciences Institute at University of California Berkeley and Lawrence Berkeley National Laboratory, Berkeley, California 94720, United States.

† These authors contributed equally to this work.

* Correspondence to: fengwang76@berkeley.edu

Abstract:

Moiré superlattices are emerging as a new route for engineering strongly correlated electronic states in two-dimensional van der Waals heterostructures, as recently demonstrated in the correlated insulating and superconducting states in magic-angle twisted bilayer graphene and ABC trilayer graphene/boron nitride moiré superlattices[1–4]. Transition metal dichalcogenide (TMDC) moiré heterostructures provide another exciting model system to explore correlated quantum phenomena[5], with the addition of strong light-matter interactions and large spin-orbital coupling. Here we report the optical detection of strongly correlated phases in semiconducting WSe_2/WS_2 moiré superlattices. Our sensitive optical detection technique reveals a Mott insulator state at one hole per superlattice site ($n = n_0$) and surprising insulating phases at fractional filling $n = 1/3n_0$ and $n = 2/3n_0$, which we assign to generalized Wigner crystallization on an underlying lattice[6–11]. Furthermore, the unique spin-valley optical selection rules[12–14] of TMDC heterostructures allow us to optically create and investigate low-energy spin excited states in the Mott insulator. We reveal an especially slow spin relaxation lifetime of many microseconds in the Mott insulating state, orders-of-magnitude longer than that of charge excitations. Our studies highlight novel correlated physics that can emerge in moiré superlattices beyond graphene.

Main text:

Moiré superlattices offer a general and powerful way to engineer correlated electronic states in van der Waals heterostructures. Consider a simplified but highly informative toy model: a two-dimensional (2D) electron gas in a periodic potential of periodicity *L*. The periodic potential leads to the formation of a set of minibands in the electron bandstructure. The electron-electron interaction *U* and the electronic bandwidth *W* of the lowest electronic miniband can be estimated as $U \sim \frac{e^2}{4\pi\varepsilon L}$ and $W \sim \frac{\hbar^2 k^2}{2m_e^*} \sim \frac{\hbar^2 \pi^2}{2m_e^* L^2}$, and the ratio U/W scales linearly with $m_e^* L$. Here ε is the effective dielectric constant, and m_e^* is the electron effective mass. Strong correlation (with U/W > 1) can be readily achieved with sufficiently large $m_e^* L$: for example, with a moiré superlattice (L ~ 10 nm) and an effective mass $m_e^* > 0.1 m_0$ for $\varepsilon \sim 4\varepsilon_0$. If the periodic moiré potential is very strong, the electron bandwidth *W* will be additionally suppressed, further enhancing the correlation effects. The design criteria of large $m_e^* L$ can be satisfied in many moiré heterostructures. One successful instance is the ABC trilayer graphene/boron nitride moiré superlattice, which exhibits tunable Mott insulator, superconductor, and correlated Chern insulator states[3,4,15]. TMDC heterostructures represent another intriguing platform. The large effective mass ($m_e^* \sim 0.5 m_0$) of TMDCs[16,17] can lead to many-body phenomena even in monolayer TMDCs[18,19], and will create particularly strong correlation effects in moiré superlattices. Further, the strong light-matter interactions[20,21] can enable optical detection and manipulation of the correlated quantum states of matter.

Here we report the observation of the Mott insulator state and generalized Wigner crystallization on an underlying lattice in semiconducting WSe_2/WS_2 moiré superlattices. Taking advantage of TMDCs' strong light-matter interactions, we optically detect both the quantum capacitance and electrical resistance of the moiré heterostructure while avoiding complications from very large

contact resistances. A prominent example of strongly correlated electronic system is the Mott insulator at one hole per superlattice site ($n = n_0$)[22,23], as illustrated in Fig. 1a. We show that the Mott insulating state exists in WSe_2/WS_2 moiré superlattices up to 45 Kelvin and has an estimated Mott-Hubbard gap of ~10 meV, an order of magnitude larger than that in graphene moiré systems. Surprisingly, we also observe additional insulating states from generalized Wigner crystallization at fractional filling $n = 1/3n_0$ and $n = 2/3n_0$. The emergence of these generalized Wigner crystal states necessitates an extended Hubbard model with not only on-site (short-range) but also inter-site (long-range) interactions[7,8]. In addition, the strong light-matter interaction and unique spin-valley selection rules allow us to optically create and detect different elementary excitations associated with the strongly correlated ground states in TMDC moiré heterostructures. We use circularly polarized light to generate a low-energy pure spin excitation, and we demonstrate an increased spin lifetime at the Mott insulating state.

In this work, we investigate correlated states in a TMDC heterostructure using a novel optically-detected resistance and capacitance (ODRC) technique. The large semiconductor bandgap in TMDCs leads to the formation of Schottky barriers at metal-TMDC junctions and correspondingly large contact resistance. This large contact resistance often hampers direct electrical transport measurements in TMDC heterostructures, particularly for low carrier doping and at low temperatures[24]. Our optical detection scheme avoids this difficulty associated with large contact resistance. For the ODRC measurements, we design a special device configuration with two regions (Fig. 1b): one half of the device has a local graphite top gate (region 1), and the other half does not (region 2). We vary the DC voltage on the local top gate (V_{top}) to continuously control the carrier doping in region 1, where the charge injection occurs with a time constant of ~ 1 s. We then add an AC excitation voltage ($\Delta\tilde{V}$) to the local top gate. For excitation

frequencies higher than 10 Hz, the electrical contact is effectively frozen and the TMDC heterostructure is floated electrically (see Methods). In this case, the AC excitation voltage only leads to charge redistribution between region 1 and region 2 with no total charge change, and the charge redistribution dynamics depends on the quantum capacitance and resistance in the moiré system. We detect the resulting change of carrier concentration in region 2 ($\Delta\tilde{n}$) optically through the induced change in optical contrast ΔOC at the intralayer exciton resonance (see Methods, Extended Data Fig. 1). The global graphite back gate is used to set the DC doping level of region 2 to optimize the exciton optical response to change in doping.

The AC electrical transport in the TMDC heterostructure can be modeled by an effective RC circuit shown in Fig. 1c. Here C_1 and C_B are the geometric capacitance between the TMDC and the top and bottom gates in region 1, respectively, and C_2 is the TMDC-bottom gate capacitance in region 2. These geometric capacitance C_i (i=1, 2, B) are set by $C_i = \frac{\varepsilon_0 \varepsilon_r A_i}{d_i}$, where ε_r is the dielectric constant of the gate dielectric, and A_i and d_i denote the relevant capacitor area and separation. The parameters to be measured are C_Q and R, which correspond to the doping-dependent quantum capacitance and resistance of the moiré superlattice in region 1, respectively. The induced optical contrast change (ΔOC) in region 2 upon an AC capacitive excitation in region 1 ($\Delta\tilde{V}$) can be obtained from the effective circuit model (see Supplementary Information) as

$$\Delta OC = \alpha \Delta\tilde{n} = \frac{\alpha}{A_2 e} \Delta\tilde{V} \left(\frac{C_1}{C_1 + C_B}\right) \frac{1}{\frac{1}{C_{eff}} + i\omega R}, \quad (1)$$

with

$$\frac{1}{C_{eff}} = \frac{1}{(C_1 + C_B)} + \frac{1}{C_2} + \frac{1}{C_Q}.$$

Here ω is the excitation frequency, e is the electron charge, and $\alpha = \Delta OC/\Delta\tilde{n}$ is the optical detection responsivity in region 2, which is a constant for the fixed bottom gate voltage in our study. The frequency-dependent optical signal ΔOC(ω) allows us to extract the values of both C_Q and R: At low excitation frequencies the resistance is negligible, so the optical signal probes the quantum capacitance C_Q, which is proportional to the density of states of the moiré heterostructure. At high modulation frequencies, both C_Q and R contribute to the optical signal.

We focus our study on near-zero twist angle WSe_2/WS_2 heterostructures, which have a moiré superlattice with period of ~ 8 nm due to the ~ 4 % lattice mismatch between the WS_2 and WSe_2 monolayers. Figure 1d shows a schematic of device D1: few-layer graphene is used for the gates and contact to the TMDC layers, and hBN is used at the top and bottom gate dielectrics (ε_r = 4.2, see Methods and Ref. [25] for fabrication details). Figure 1e shows the optical microscopy image of the final device, with contours highlighting the WS_2 and WSe_2 layers and the local graphite top gate. To verify the presence of the moiré superlattice, we examine the optical absorption spectrum of the heterostructure (Fig. 1f). It shows clear splitting of the WSe_2 A exciton, which is a signature of the moiré superlattice in the heterostructure[25].

Figure 2a shows the ODRC signals as a function of the hole doping of the WSe_2/WS_2 moiré superlattice in region 1. We use an AC excitation voltage with the peak-to-peak amplitude of 10 mV at 1 kHz and 30 kHz. When region 1 is near charge neutral (V_{top} > 0.2 V), the ΔOC signal is small because no carriers are available to redistribute in the bandgap of WSe_2. When region 1 is hole doped (V_{top} < 0.2 V), charge redistribution occurs, leading to a large increase in signal. Interestingly, we observe a strong gap-like feature at -1 V (blue dashed line in Fig. 2a). From a capacitance model, we estimate the corresponding hole concentration to be 1.86 x 10^{12} cm^{-2}, which matches well with the density of one hole per moiré unit cell (n_0 = 1.88 x 10^{12} cm^{-2}, see

Methods). We also observe two sharp dips at -0.2 V and -0.6 V (orange and green dashed lines in Fig. 2a), which correspond to hole concentrations of $n = n_0/3$ and $n = 2n_0/3$, respectively. Additionally, a broad, weaker feature is observed at -2.25 V, corresponding to $n = 2n_0$. These features become stronger at higher excitation frequency of 30 kHz. The ODRC signals for additional aligned heterostructures are shown in Extended Data Fig. 5.

We extract numerical values for the doping-dependent C_{eff} and R of the moiré heterostructure based on the effective AC circuit model and Eq. 1. We plot C_{eff} and R as a function of carrier doping in Fig. 2b and 2c (grey lines), respectively. The optical responsivity of $\alpha = 1.4 \times 10^{-12}$ cm^2 is chosen so that $\frac{1}{C_{eff}} = \frac{1}{(C_1+C_B)} + \frac{1}{C_2}$ at high doping, where the quantum capacitance is much larger than the geometry capacitances and has negligible contribution. At $n = n_0$, $n = n_0/3$, and $n = 2n_0/3$, C_{eff} decreases while the geometric capacitances remain unchanged (Fig. 2b). This decrease of C_{eff} is due to a much smaller quantum capacitance C_Q, which results from significantly reduced density of states at these fillings. At the same time, the electrical resistance shows marked increases at $n = n_0$, $n = n_0/3$, and $n = 2n_0/3$ (Fig. 2c). The simultaneous reduction of the density of state and large increase of the resistance indicate the emergence of insulating states at these fillings.

To quantitatively test our effective circuit model, we measure the frequency dependence of the ODRC signal at several representative hole-doping densities. Figure 2d displays the experimental data (symbols). We observe clear signal fall-off with increasing frequency, and data can be reproduced by the circuit model prediction (solid lines). The extracted effective capacitance and resistance at these fillings from the frequency dependence (black dots in Fig. 2b and 2c) agree well with the values extracted directly from the data in Fig. 2a.

Our results show that the WSe_2/WS_2 moiré heterostructure hosts insulating states with reduced density of states and increased resistance at $n = n_0$, $n = n_0/3$, and $n = 2n_0/3$. These features are completely absent in large twist angle WSe_2/WS_2 heterostructures (see Methods, Extended Data Fig. 6) and only emerge in the moiré superlattices. The insulating state at $n = n_0$ is typically assigned to a Mott insulator[22,23], but may also be considered to be an interaction-driven Wigner crystal state[6–11] or a charge transfer insulator[26] (Fig. 2e). This state corresponds to half filling of the moiré miniband because TMDC heterostructure has a degeneracy of 2 from spin-valley locking[13]. Similar correlated insulating states have also been observed at $n = n_0$ in twisted bilayer graphene and ABC trilayer graphene/boron nitride moiré superlattices[1–4].

On the other hand, the observation of insulating states at $n = n_0/3$ and $n = 2n_0/3$ is quite surprising. Insulating states at fractional filling of the lattice sites have not been observed in other moiré superlattice systems and cannot be described as a Mott insulator or by a Hubbard model with only on-site repulsive interactions. We hypothesize that these insulating states at $n = n_0/3$ and $n = 2n_0/3$ correspond to generalized Wigner crystallization[6–11] of holes in the TMDC moiré superlattice. Figure 2e illustrates the real-space configurations of the generalized Wigner crystal states, where holes try to avoid not only double-occupation in one site, but also simultaneous occupation of adjacent sites. There are three degenerate Wigner crystallization configurations. The TMDC moiré system spontaneously breaks the lattice translational symmetry due to the electron-electron interactions and condenses to one specific configuration with a $\sqrt{3} \times \sqrt{3}$ charge density wave pattern. The emergence of these generalized Wigner crystal states suggests that even the inter-site (long-range) interaction energy is larger than the moiré miniband bandwidth, confirming the very strong correlation in the TMDC moiré heterostructure.

We perform the ODRC measurements of the doping-dependent quantum capacitance and resistance of the TMDC moiré superlattices at different temperatures. Fig. 3a shows the extracted resistance for temperatures from 3 K to 70 K. The resistance peaks of the Mott insulator and generalized Wigner crystal states are observable up to temperatures of 45 K and 10 K, respectively. We estimate the Mott-Hubbard gap to be $\Delta \sim 10$ meV by fitting the resistance to a thermal activation function $\exp[-\Delta/(2k_BT)]$ for the Mott insulator state at $n = n_0$ (black dashed line in Fig. 3b). Due to the limited range exhibiting thermal activation behavior, the estimated Mott gap has relatively large uncertainty. It is difficult to estimate the size of the insulating gaps of the generalized Wigner crystal states from the experimental data, but they are likely to be 5-10 times smaller than the Mott insulator gap based on the temperature at which the generalized Wigner crystal signatures disappear.

The strong electron-correlation and light-matter-interaction in the heterostructure provides unique opportunities to optically investigate excited states from the correlated phases, such as low-energy charge and spin excitations. Charge excitations in Mott insulator systems have been intensively studied, featuring ultrafast decay dynamics (typically few picoseconds) from the holon-doublon recombination process[27–29]. On the other hand, the dynamics of pure spin-excitations have been difficult to explore. Here we directly measure the doping-dependent decay of a pure spin excitation by taking advantage of the unique spin-valley selection rules in the TMDC heterostructure[12–14]. We use the pump-probe scheme described in Ref. [30,31] to generate and probe the spin excitation in the moiré heterostructure at 20 K. Specifically, a circularly polarized pump excitation is employed to selectively excite K-valley excitons composed of spin-up holes and electrons. The relaxation of the spin-polarized electrons and holes within about 100 ns results in a residual spin polarization in the Mott insulator lower

Hubbard band, as illustrated in Fig. 4a. We probe the evolution of the residual spin polarization through the pump-induced circular dichroism signal and the charge population through the pump-induced change in total absorption of a probe beam. Figure 4b shows the time evolution of the spin population at different hole densities. The doping-dependent spin lifetime, summarized as blue symbols in Fig. 4c, shows a prominent increase at the Mott insulator state ($n = n_0$) and reaches more than 8 us. In contrast, the lifetime of charge excitations (black symbols) is orders-of-magnitude shorter. The long-lived spin excitations from the Mott insulator state can provide important information about its spin configuration. It has been proposed that the Mott insulator state in the WSe_2/WS_2 moiré superlattice can host intriguing spin states such as quantum spin liquid[32,33]. However, further theoretical studies will be required to understand the experimentally observed spin dynamics in the Mott insulating state, which is beyond the scope of this paper.

Our results demonstrate the TMDC moiré heterostructures can host novel quantum correlated phases and offer an attractive platform for probing excited state and non-equilibrium dynamics of the correlated phases due to a unique combination of highly correlated electrons, strong light-matter interactions, and large spin-orbital effect in the system.

References:

1. Cao, Y. *et al.* Correlated insulator behaviour at half-filling in magic-angle graphene superlattices. *Nature* **556**, 80–84 (2018).
2. Cao, Y. *et al.* Unconventional superconductivity in magic-angle graphene superlattices. *Nature* **556**, 43–50 (2018).
3. Chen, G. *et al.* Evidence of a gate-tunable Mott insulator in a trilayer graphene moiré superlattice. *Nat. Phys.* **15**, 237–241 (2019).
4. Chen, G. *et al.* Signatures of tunable superconductivity in a trilayer graphene moiré superlattice. *Nature* **572**, 215–219 (2019).
5. Wu, F., Lovorn, T., Tutuc, E. & MacDonald, A. H. Hubbard Model Physics in Transition Metal Dichalcogenide Moire Bands. *Phys. Rev. Lett.* **121**, 26402 (2018).
6. Wigner, E. On the Interaction of Electrons in Metals. *Phys. Rev.* **46**, 1002–1011 (1934).
7. Hubbard, J. Generalized Wigner lattices in one dimension and some applications to tetracyanoquinodimethane (TCNQ) salts. *Phys. Rev. B* **17**, 494–505 (1978).
8. Wu, C., Bergman, D., Balents, L. & Das Sarma, S. Flat Bands and Wigner Crystallization in the Honeycomb Optical Lattice. *Phys. Rev. Lett.* **99**, 70401 (2007).
9. Hiraki, K. & Kanoda, K. Wigner Crystal Type of Charge Ordering in an Organic Conductor with a Quarter-Filled Band: (D1-DCNQI)2Ag. *Phys. Rev. Lett.* **80**, 4737–4740 (1998).
10. Padhi, B., Setty, C. & Phillips, P. W. Doped Twisted Bilayer Graphene near Magic Angles: Proximity to Wigner Crystallization, Not Mott Insulation. *Nano Lett.* **18**, 6175–6180 (2018).
11. Padhi, B. & Phillips, P. W. Pressure-induced metal-insulator transition in twisted bilayer graphene. *Phys. Rev. B* **99**, 1–9 (2019).
12. Mak, K. F., He, K., Shan, J. & Heinz, T. F. Control of valley polarization in monolayer MoS_2 by optical helicity. *Nat. Nanotechnol.* **7**, 494–498 (2012).
13. Xiao, D., Liu, G.-B., Feng, W., Xu, X. & Yao, W. Coupled Spin and Valley Physics in Monolayers of MoS_2 and Other Group-VI Dichalcogenides. *Phys. Rev. Lett.* **108**, 196802 (2012).
14. Cao, T. *et al.* Valley-selective circular dichroism of monolayer molybdenum disulphide. *Nat. Commun.* **3**, 887 (2012).
15. Chen, G. *et al.* Tunable Correlated Chern Insulator and Ferromagnetism in Trilayer Graphene/Boron Nitride Moire Superlattice. arXiv:1905.06535 (2019).
16. Kadantsev, E. S. & Hawrylak, P. Electronic structure of a single MoS_2 monolayer. *Solid State Commun.* **152**, 909–913 (2012).
17. Fallahazad, B. *et al.* Shubnikov--de Haas Oscillations of High-Mobility Holes in Monolayer and Bilayer WSe_2 Landau Level Degeneracy, Effective Mass, and Negative Compressibility. *Phys. Rev. Lett.* **116**, 86601 (2016).
18. Roch, J. G. *et al.* Spin-polarized electrons in monolayer MoS_2. *Nat. Nanotechnol.* **14**, 432–436 (2019).
19. Back, P. *et al.* Giant Paramagnetism-Induced Valley Polarization of Electrons in Charge-Tunable Monolayer $MoSe_2$. *Phys. Rev. Lett.* **118**, 1–5 (2017).
20. Splendiani, A. *et al.* Emerging Photoluminescence in Monolayer MoS_2. *Nano Lett.* **10**, 1271–1275 (2010).
21. Mak, K. F., Lee, C., Hone, J., Shan, J. & Heinz, T. F. Atomically thin MoS_2: A new

direct-gap semiconductor. *Phys. Rev. Lett.* **105**, 2–5 (2010).
22. Mott, N. F. The Basis of the Electron Theory of Metals, with Special Reference to the Transition Metals. *Proc. Phys. Soc. Sect. A* **62**, 416–422 (1949).
23. Imada, M., Fujimori, A. & Tokura, Y. Metal-insulator transitions. *Rev. Mod. Phys.* **70**, 1039–1263 (1998).
24. Allain, A., Kang, J., Banerjee, K. & Kis, A. Electrical contacts to two-dimensional semiconductors. *Nat. Mater.* **14**, 1195 (2015).
25. Jin, C. *et al.* Observation of moiré excitons in WSe_2/WS_2 heterostructure superlattices. *Nature* **567**, 76–80 (2019).
26. Zhang, Y., Yuan, N. F. Q. & Fu, L. Moire quantum chemistry: charge transfer in transition metal dichalcogenide superlattices. arXiv:1910.14061 (2019).
27. Prelovs, P. & Lenarc, Z. Ultrafast Charge Recombination in a Photoexcited Mott-Hubbard Insulator. *Phys. Rev. Lett.* **111**, 16401 (2013).
28. Cuo, N. *et al.* Photoinduced transition from Mott insulator to metal in the undoped cuprates. *Phys. Rev. B* **83**, 125102 (2011).
29. Giannetti, C. *et al.* Ultrafast optical spectroscopy of strongly correlated materials and high-temperature superconductors: a non-equilibrium approach. *Adv. Phys.* **65**, 58–238 (2016).
30. Kim, J. *et al.* Observation of ultralong valley lifetime in WSe_2/MoS_2 heterostructures. *Sci. Adv.* **3**, e1700518 (2017).
31. Jin, C. *et al.* Imaging of pure spin-valley diffusion current in WS_2/WSe_2 heterostructures. *Science* **360**, 893–896 (2018).
32. Law, K. T. & Lee, P. A. 1T-TaS as a quantum spin liquid. *Proc. Natl. Acad. Sci.* **114**, 6996–7000 (2017).
33. Grover, T., Trivedi, N., Senthil, T. & Lee, P. A. Weak Mott insulators on the triangular lattice: Possibility of a gapless nematic quantum spin liquid. *Phys. Rev. B* **81**, 245121 (2010).

Acknowledgements: We thank Shaowei Li for the discussions, Sheng Wang for help with device fabrication, and Conrad Stansbury and Caitlin Wang for their assistance with figure design. This work was supported primarily by the U.S. Department of Energy, Office of Science, Office of Basic Energy Sciences, Materials Sciences and Engineering Division under Contract no. DE-AC02-05-CH11231 (van der Waals heterostructures program, KCWF16). This work was also supported by the US Army Research Office under MURI award W911NF-17-1-0312. E.C.R. acknowledges support from the Department of Defense (DoD) through the National Defense Science & Engineering Graduate Fellowship (NDSEG) Program. C.J. acknowledges support from a Kavli Postdoctoral Fellowship. S.T. acknowledges support from NSF DMR-1552220 and 1838443.

Author contributions: E.C.R., D.W., and C.J. contributed equally. F.W. conceived the research. E.C.R, D.W., and C.J. carried out optical measurements. D.W., E.C.R, C.J., F.W. performed data analysis. E.C.R., D.W., B.G., X.W., M.I.B.U, S.Z., W.Z., Z.Z., J. C., M. C., A.Z. contributed to the fabrication of van der Waals heterostructures. K.Y., M.B., and S.T. grew WSe_2 and WS_2 crystals. K.W. and T.T. grew hexagonal boron nitride crystals. All authors discussed the results and wrote the manuscript.

Author information: The authors declare no competing interests. Correspondence and requests for materials should be addressed to fengwang76@berkeley.edu.

Main figures:

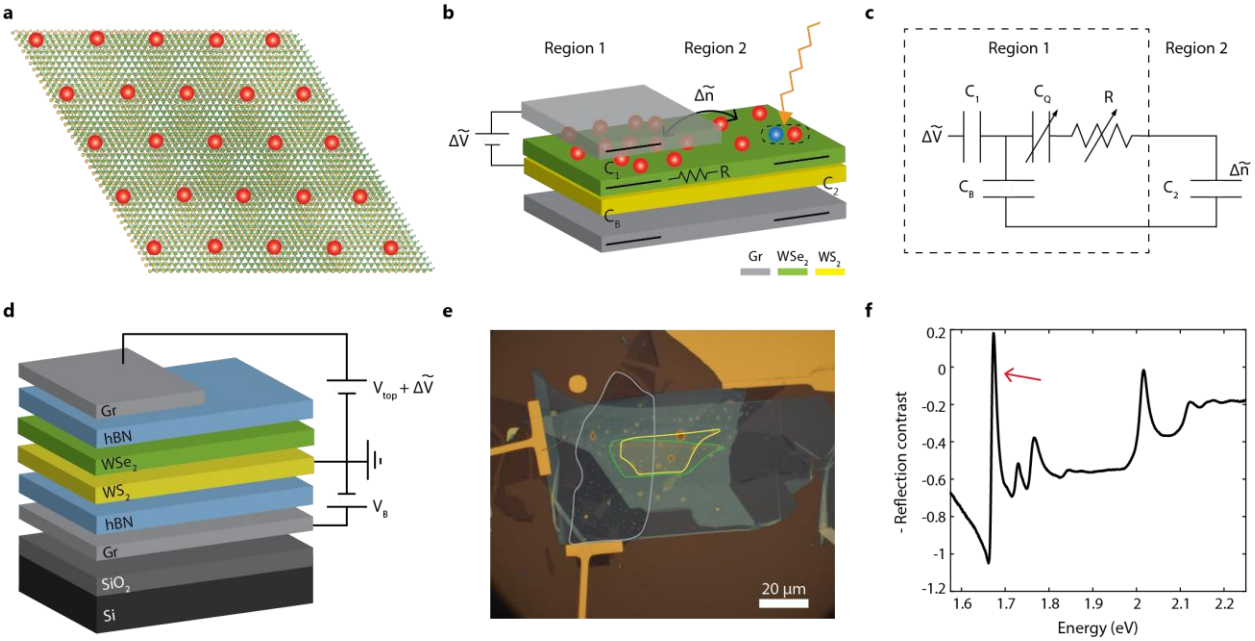

Fig. 1 | Optically detected resistance and capacitance (ODRC) technique in WSe_2/WS_2 superlattice. (**a**) Illustration of a Mott insulator state in a WSe_2/WS_2 moiré superlattice with one hole per superlattice unit cell. (**b** and **c**) Device schematic for an ODRC measurement in a WSe_2/WS_2 heterostructure (**b**), which includes a local top gate and global back gate. A small AC bias $\Delta\tilde{V}$ leads to charge redistribution between region 1 and region 2 ($\Delta\tilde{n}$), which is detected via the change in optical reflectivity of the WSe_2 exciton in region 2. This AC measurement can be modeled as an effective RC circuit (**c**), where the elements are shown schematically in (**b**). C_1, C_B, and C_2 are the illustrated geometric capacitances in the system, and R and C_Q are the doping-dependent resistance and quantum capacitance of region 1 that we measure. (**d** and **e)** Side-view illustration (**d**) and optical microscope image (**e**) of near-zero twist angle heterostructure, device D1. The graphite top gate, WS_2, and WSe_2 flakes are outlined in grey, yellow, and green, respectively. (**f**) Optical absorption spectrum of the heterostructure showing splitting of the WSe_2 A exciton into three prominent peaks, which is characteristic of intralayer moiré excitons in an aligned heterostructure. The ODRC measurements use a laser probe in resonance with the lowest energy exciton peak (red arrow).

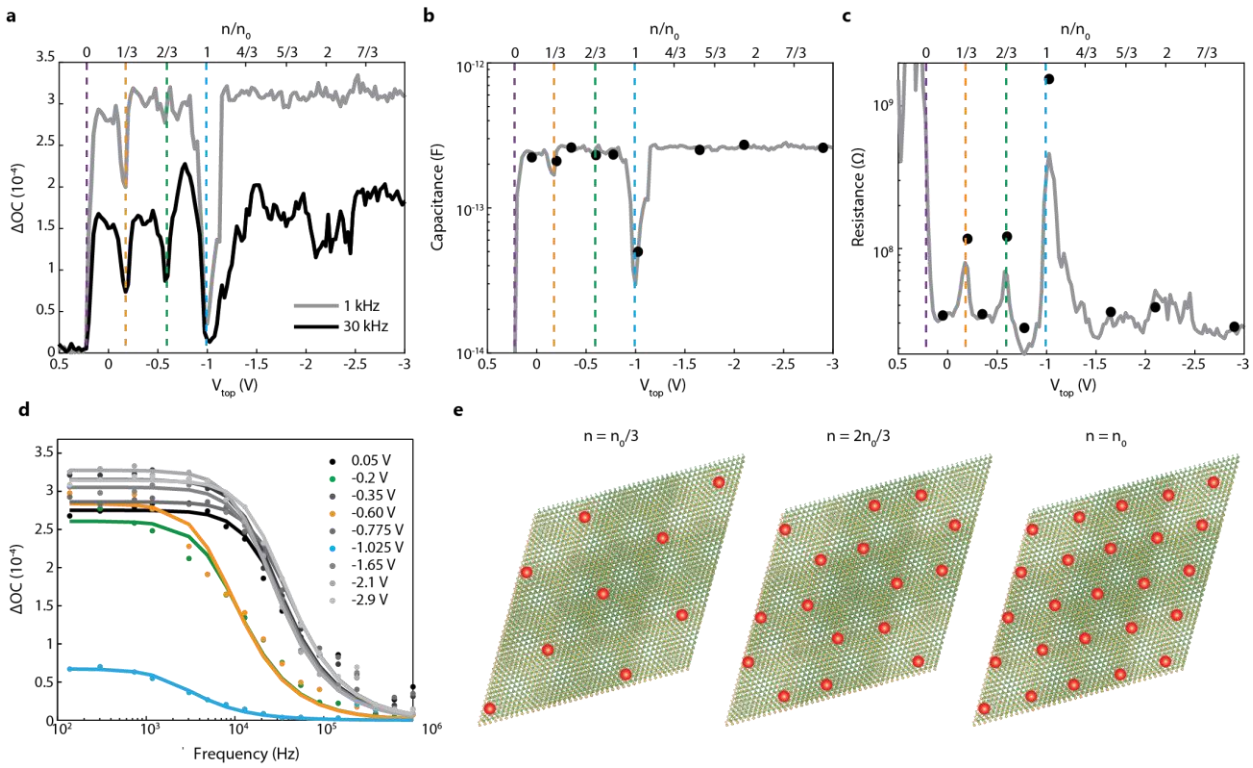

Fig. 2 | Doping-dependent resistance and capacitance probed by ODRC. (**a**) ODRC signal at 1 kHz (grey) and 30 kHz (black) from charge neutral to moderate hole doping. Strong gap-like features are observed at hole doping levels of $n = n_0/3$ (orange dashed line), $n = 2n_0/3$ (green dashed line), and $n = n_0$ (blue dashed line). The purple dashed line corresponds to n = 0. (**b**-**d**) Extracted capacitance C_{eff} (**b**) and resistance (**c**) of region 1 from the data in (**a**) (grey curves) and from the frequency-dependent ODRC signal (**d**) at representative doping levels (black dots). The decreased capacitance and increased resistance indicate emerging insulating states at $n = n_0/3$, $n = 2n_0/3$, and $n = n_0$. All measurements are done at 3 K. (**f**) Illustrations of generalized Wigner crystal ($n = n_0/3$, $n = 2n_0/3$) and Mott insulator states ($n = n_0$) in a WSe_2/WS_2 moiré superlattice.

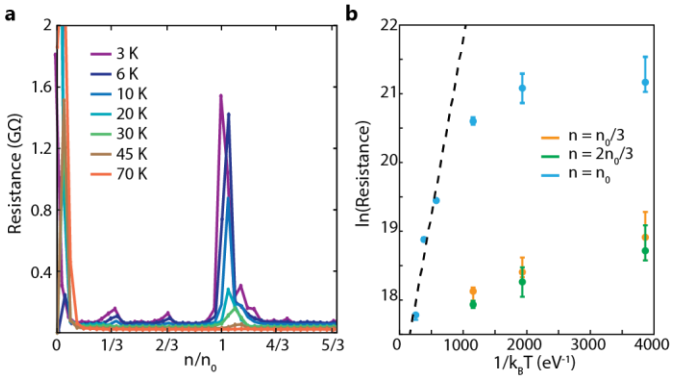

Fig. 3 | Temperature dependence of Mott and generalized Wigner crystal states. (**a**) Extracted resistance from ODRC measurements taken at a range of temperatures between 3 K and 70 K. The Mott insulator state at $n = n_0$ is observable up to 45 K, and the generalized Wigner crystal states at $n = n_0/3$ and $n = 2n_0/3$ persist until 10 K. (**b**) Plot of ln(Resistance) versus $1/k_BT$ for Mott (blue) and generalized Wigner crystal states (orange and green). Error bars correspond to the estimated uncertainty in the extracted resistance values. The estimated thermal activation gap for the Mott state is ~ 10 meV, which is found by fitting the data in (b) to a thermal activation function (black dashed line).

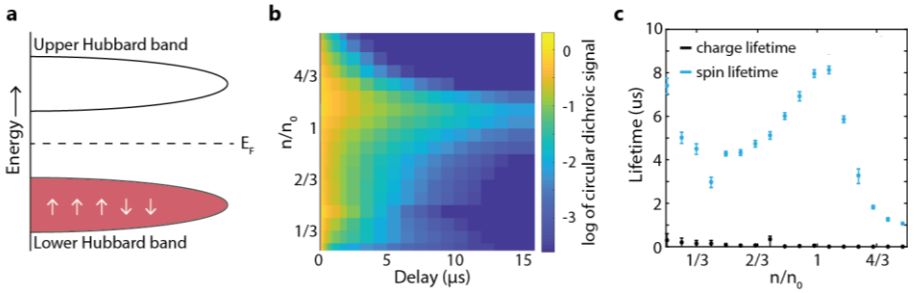

Fig. 4 | Optical investigation of low-energy spin excitation dynamics of a WSe_2/WS_2 Mott insulator. (**a**) A circularly polarized pump pulse selectively excites K-valley excitons with spin-up electrons and holes in the moiré heterostructure. After a fast charge recombination process, an excess of spin-polarized holes remains in the lower Hubbard band. The evolution of this low-energy spin excitation can be measured by a second probe pulse through pump-induced circular dichroic signals. (**b**) Doping dependent decay dynamics of the optically generated pure spin excitations. (**c**) Summary of the spin (blue) and charge (black) lifetimes as a function of hole doping. The spin relaxation slows down markedly near $n = n_0$, with a lifetime as long as 8 μs. On the other hand, the total charge population decays quickly for all doping levels.

Methods:

ODRC measurements:

A function generator (Rigol 1022Z) is used to generate the top gate voltage consisting of a DC offset, V_{top}, with small AC modulation, $\Delta\tilde{V}$. A voltage source (Keithley 2400) is used for the back gate voltage. A laser diode with center energy of 1.66 eV serves as the probe light. The diode energy is fine-tuned using a thermoelectric cooler, so that the probe energy is resonant with the lowest energy WSe_2 A exciton absorption peak in region 2. The reflected probe light is collected with an avalanche photo diode (Thorlabs APD 410A) and then analyzed using a lock-in amplifier that is locked to the function generator output.

WSe_2 A exciton absorption in region 2:

The lowest-energy WSe_2 A exciton in region 2 is used to measure the electrical properties of region 1 as the local top gate is tuned. To be a reliable probe, the exciton in region 2 should only respond to charge redistribution due to the modulation voltage $\Delta\tilde{V}$, but not to the DC bias applied to the local top gate, V_{top}. We measure the optical spectrum of the lowest-energy WSe_2 A exciton (between 1.6 to 1.74 eV) while sweeping V_{top} from 0.5 V to -3.5 V (Extended Data Fig. 1a). We record the spectrum 15 s after changing V_{top} to ensure the contact injects charge. We observe almost no change in the spectrum. Therefore, the static local top gate does not influence the hole concentration in region 2, and it remains a stable probe for all V_{top} used.

We measure the absorption spectrum as a function of the carrier density in region 2 by varying the global back gate voltage. Extended Data Fig. 1b shows the absorption spectra when the back gate voltage is tuned in a small range around -1 V. For the ODRC measurement, the modulation voltage $\Delta\tilde{V}$ is typically set to 10-25 mV, so the redistributed

charges correspond to a small back gate voltage change of <25 mV. Within this range, the exciton resonance (1.673 eV) shows monotonic and linear change with carrier concentration. Therefore, α is a constant for our choice of back gate voltage.

We estimate an optical detection responsivity α of ~ 1.4 x 10^{-12} cm^2. The noise of the ODRC signal is at ~ 2 x 10^{-6} level in our lock-in measurement for 3 s average time. It allows us to detect a carrier density change in region 2 as small as 10^6 cm^{-2} with optical detection.

Low-frequency behavior of ODRC signal:

Extended Data Fig. 2 shows the frequency-dependent ODRC signal at V_{top} = -1.6 V (i.e. away from any features) for modulation frequencies between 0.05 Hz to 137 Hz. The carrier injection through the graphite contact has a characteristic time constant of ~ 1s. At the lowest modulation frequency (0.05 Hz), the graphite contact can efficiently inject charge in response to $\Delta\tilde{V}$. As a result, the carrier density in region 2 remains constant and the overall ODRC signal is negligible. At 1 Hz, the ODRC signal is partially reduced compared with higher frequency responses because the contact can inject some charge in response to $\Delta\tilde{V}$. For frequencies higher than ~10 Hz, the contact becomes frozen. As a result, the heterostructure is effectively floated and the ODRC signal reaches its typical low-frequency value. We also note that the ODRC signal is linear with $\Delta\tilde{V}$.

Heterostructure preparation for optical measurements:

We use a dry transfer method with a polyethylene terephthalate (PET) stamp to fabricate the WSe_2/WS_2 heterostructures[34]. Monolayer WSe_2, monolayer WS_2, few-layer graphene, and thin hBN flakes are first exfoliated onto Si substrates with a 90 nm SiO_2 layer. For aligned heterostructure, we use polarization-dependent second harmonic generation (SHG) to determine

the crystal axes of WS_2 and WSe_2[35,36]. We then use a PET stamp to pick up the few-layer graphene top gate, top hBN flake, the WS_2 monolayer, the WSe_2 monolayer, the few-layer graphene contact, the bottom hBN flake, and the few-layer graphene back gate in sequence. Between picking up WS_2 and WSe_2, we adjust the angle of the PET stamp to ensure a near-zero twist angle between the flakes. The PET stamp with the above heterostructure is then stamped onto a clean Si substrate with 90 nm SiO_2. The PET and samples are heated to 60 °C during the pick up and to 130 °C for the stamp process. Finally, we dissolve the PET in dichloromethane overnight at room temperature. Contacts (~75 nm gold with ~5 nm chromium adhesion layer) to the few-layer graphene flakes are made using electron-beam lithography and electron-beam evaporation. Finally, we measure polarization-dependent SHG on the monolayer TMDCs in the heterostructure to determine the twist angle (see Extended Data Fig. 4).

Calibration of hBN dielectric constant:

We directly calibrated the hBN dielectric constant against the known SiO_2 dielectric constant using a dual-gate TMDC device with a graphite top gate (with hBN as the gate dielectric) and a Si back gate (with SiO_2 as the gate dielectric). Specifically, we fabricated a dual gated $MoSe_2$ device with a 45 nm thick top hBN gate and 290 nm SiO_2/Si back gate. The hBN crystal is from the same batch that was used to fabricate our WSe_2/WS_2 moiré heterostructure devices. Extended Data Fig. 3a shows the $MoSe_2$ A exciton peak intensity as a function of the top and back gate voltages. Extended Data Fig. 3b shows the extracted charge neutral points for each Si back gate, which corresponds to the top graphite gate voltage that brings the system to zero net charge. The data shows linear behavior, where the slope indicates the relative gate efficiency. The hBN dielectric constant is then obtained using a parallel plate capacitor model. The hBN thickness was determined by calibrated atomic force microscopy measurements, and the SiO_2 thickness

was verified by the optical reflection spectrum. We obtain an hBN dielectric constant of 4.2 ± 0.4 using the SiO_2 dielectric constant of 3.9.

Determination of the relative twist angle between WSe_2 and WS_2 layers:

The twist angle between the WSe_2 and WS_2 flakes in the device in the main text, D1, is 0.4 ± 0.3 degrees, as determined via polarization-dependent SHG (Extended Data Fig. 4)[25,35-36]. The SHG signal is four times larger on the heterostructure than on the monolayer regions, indicating that this device is close to 0 degrees, rather than 60 degrees.

Determination of moiré density n_0:

The moiré density n_0 corresponds to one hole per moiré unit cell, and it is directly determined by the moiré periodicity through $n_0 = 1/(L_M^2 \sin \pi/3)$. Here $L_M = a/\sqrt{\delta^2 + \theta^2}$ is the moiré superlattice constant, $\delta = (a - a')/a \approx 4\%$ is the lattice mismatch between WSe_2 (a = 0.328 nm) and WS_2 (a' = 0.315 nm), and θ is the twist angle between the two layers. At θ < ~1 degree, L_M is mainly determined by the intrinsic lattice constant mismatch between the two layers, so n_0 is not sensitive to a small uncertainty in θ. For the device in the main text, D1, we measured θ to be 0.4 ± 0.3 degrees from angle-dependent SHG. This corresponds to $n_0 = 1.88 \times 10^{12}$ cm^{-2} with an uncertainty of ~10%.

ODRC results from additional near-aligned heterostructures:

We measured three near-aligned WSe_2/WS_2 moiré heterostructures (twist angle <1 degree). Extended Data Fig. 5a and 5b show the ODRC signal of the other two devices D2 and D3, respectively. The qualitative behavior of the Mott insulator and generalized Wigner crystal states that are observed in D1 and described in the text is reproducible in these devices. We observe clear increase in resistance and decrease in ΔOC signal at the Mott states and the generalized

Wigner crystal state at $n = 1/3n_0$. The generalized Wigner crystal state at $n = 2/3n_0$, however, is almost not observable. We do notice that device D2 and D3 have much larger inhomogeneous broadening compared with device D1, as characterized by the much broader width of the resistance peak. Presumably, the $n = 2/3n_0$ state is much more fragile than the Mott insulator and the $n = 1/3n_0$, and it is completely smeared out by larger inhomogeneous broadening in D2 and D3.

ODRC signal in large twist angle WSe_2/WS_2 heterostructure:

We measured the ODRC signal for a large twist angle WSe_2/WS_2 heterostructure, D4. In this device, the monolayer WSe_2 and WS_2 flakes are intentionally misaligned, and the absorption spectrum is characteristic of a large twist angle heterostructure. The signal from misaligned heterostructure also shows sharp increase when doped below the bandgap (red curve in Extended Data Fig. 6a), indicating that charge redistribution occurs. However, the signal is largely flat and does not show any clear dips corresponding to insulating states, in sharp contrast with the aligned case (blue curve). This observation is consistent with our conclusion that the insulating states in an the aligned heterostructure are Mott and generalized Wigner states in the moiré superlattice, which is not present in a large twist angle heterostructure. Extended Data Fig. 6b shows the ODRC signal at several representative frequencies, showing a characteristic RC circuit fall-off with increasing frequency. No additional feature is observed in the hole-doping region up to the frequency of 1 MHz, further confirming the absence of insulating states. The overall lower resistance in the misaligned device may be due to the difference in back gate doping used in the two measurements.

Generation of optical pump-probe pulses with controlled time delay:

Two electronic pulse generators (HP 8082A and HP 214B) are used to generate optical pump and probe pulses separately. Both pulse generators are triggered by the digital output of a data acquisition card, so the period and delay of the two triggering signals can be directly controlled with computer. The output electronic pulses with ~ 20 nanosecond pulse duration are then converted to optical pulses by two RF-coupled laser diode modules, with energies at 1.80 eV (pump) and 1.66 eV (probe), respectively. The pump and probe beams are focused at the sample with diameters of ~ 30 um and ~ 5 um, respectively. Their polarizations are set with linear polarizers and a shared quarter wave plate. The reflected probe light is collected by a photomultiplier tube. The pump-probe signal is analyzed using a lock-in amplifier at a ~ 2.5 kHz modulation frequency.

Method references:

34. Wang, L. *et al.* One-Dimensional Electrical Contact to a Two-Dimensional Material. *Science* **342**, 614–617 (2013).
35. Kumar, N. *et al.* Second harmonic microscopy of monolayer MoS_2. *Phys. Rev. B* **87**, 161403 (2013).
36. Li, Y. *et al.* Probing Symmetry Properties of Few-Layer MoS_2 and h-BN by Optical Second-Harmonic Generation. *Nano Lett.* **13**, 3329–3333 (2013).

Data and materials availability: The data that support the findings of this study are available from the corresponding author upon reasonable request.

Extended data figures:

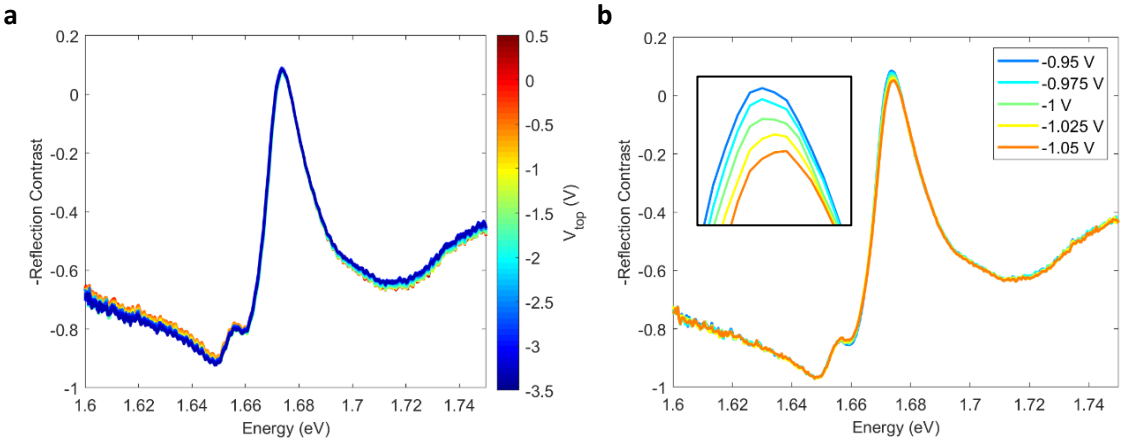

Extended Data Fig. 1. | WSe2 A exciton gate behavior. (**a**) Reflection contrast spectra for the lowest-energy WSe_2 A exciton resonance in region 2 of device D1 when the local top gate voltage V_{top} is tuned from 0.5 V to -3.5 V. Region 2 is not affected when the hole concentration is tuned in region 1 by V_{top}. (**b**) Reflection contrast spectra for the WSe_2 A exciton in region 2 when the global back gate is tuned from -0.95 V to -1.05 V. Inset shows zoomed-in view of the exciton peak. The spectral change is monotonic and approximately linear with carrier concentration.

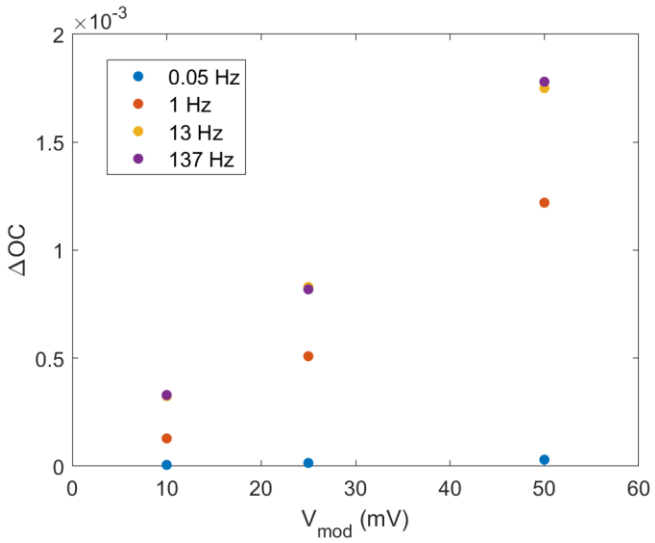

Extended Data Fig. 2. | ODRC signal measured at very low frequencies for a range of modulation voltages.

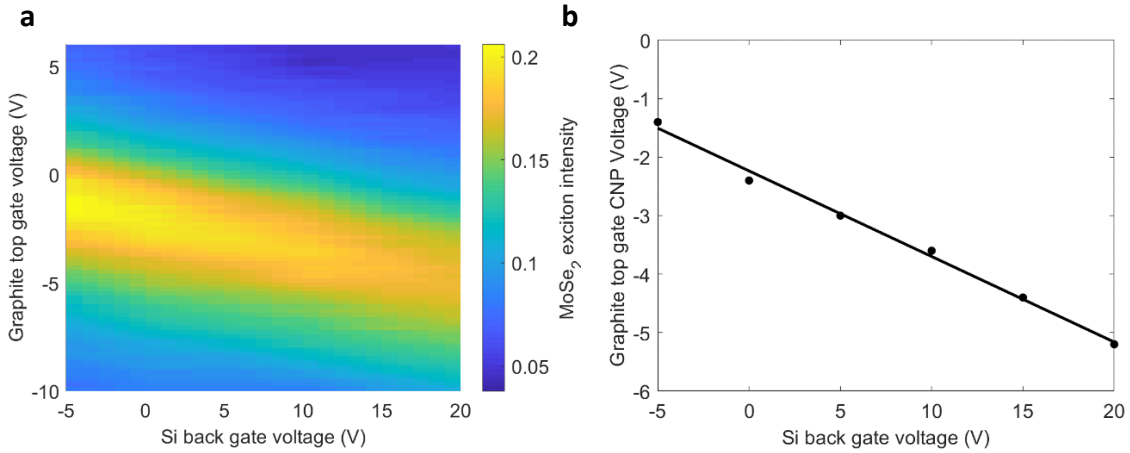

Extended Data Fig. 3. | Calibration of hBN dielectric constant. (**a**) $MoSe_2$ A exciton peak intensity as the top graphite gate and back Si gate voltages are tuned. (**b**) The extracted charge neutral points, CNP, (dots) for each Si back gate, corresponding to the top graphite gate voltage that brings the system to zero net charge. The black line is a linear fit to the data, from which the relative gate efficiency is determined.

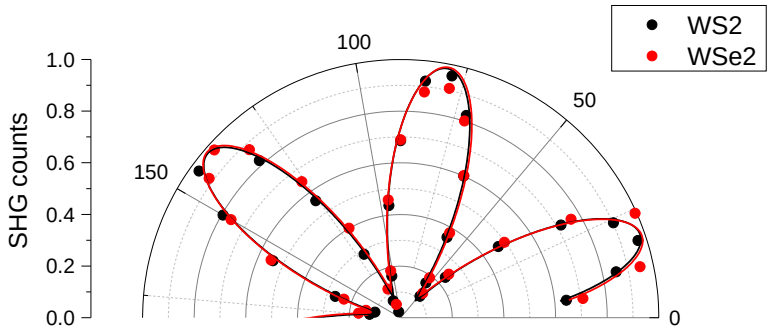

Extended Data Fig. 4. | Determination of WSe_2 and WS_2 flake alignment. Polarization-dependent SHG signal on monolayer WSe_2 (red circles) and WS_2 (black circles) regions of device D1 and corresponding fittings (red and black curves).

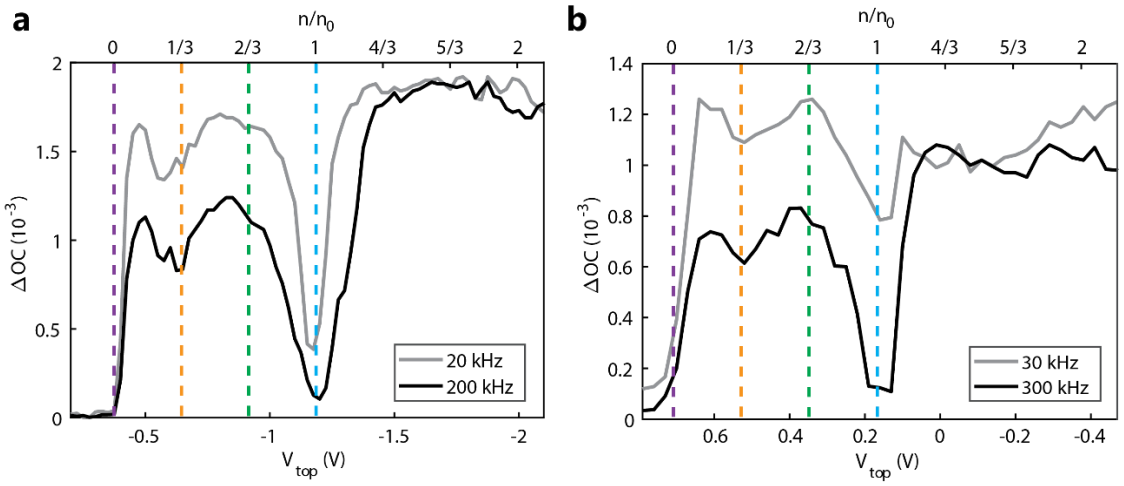

Extended Data Fig. 5. | ODRC signal for additional aligned WSe_2/WS_2 heterostructures. ODRC signal at low (grey) and high (black) frequency from charge neutral to moderate hole doping in devices D2 (**a**) and D3 (**b**). The dashed lines are guides to the eye at n = 0 (purple), n = $n_0/3$ (orange), n = $2n_0/3$ (green), and n = n_0 (blue).

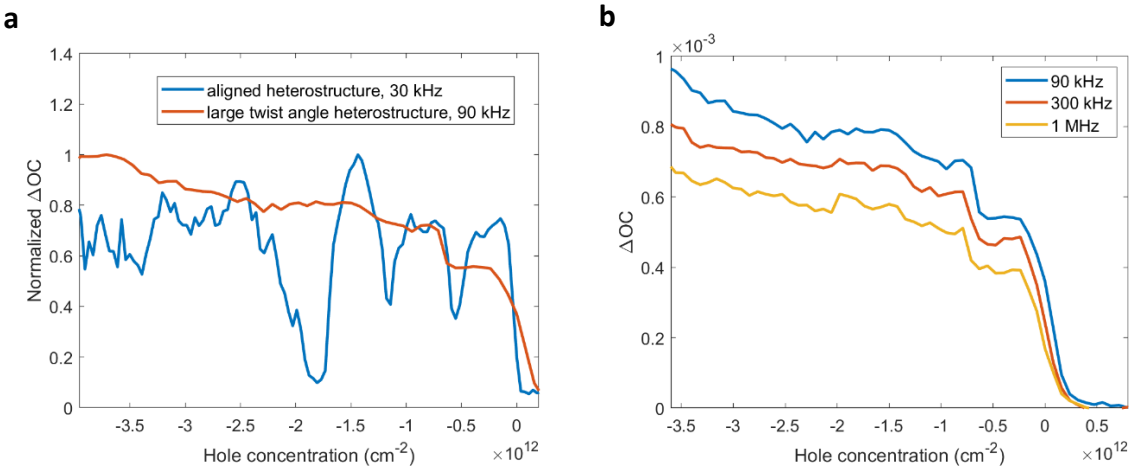

Extended Data Fig. 6. | ODRC signal for large twist angle WSe_2/WS_2 heterostructure. (**a**) Normalized ΔOC for a large twist angle heterostructure D4 (blue) and aligned heterostructure D1 (black). The misaligned heterostructure does not show any insulating features. (**b**) The frequency dependence of the large twist angle signal shows a characteristic RC circuit fall-off with increasing frequency.

Supplementary Information for

Mott and generalized Wigner crystal states in WSe_2/WS_2 moiré superlattices

Emma C. Regan†, Danqing Wang†, Chenhao Jin†, M. Iqbal Bakti Utama, Beini Gao, Xin Wei, Sihan Zhao, Wenyu Zhao, Zuocheng Zhang, Kentaro Yumigeta, Mark Blei, Johan Carlstroem, Kenji Watanabe, Takashi Taniguchi, Sefaattin Tongay, Michael Crommie, Alex Zettl, Feng Wang*

† These authors contributed equally to this work

* Correspondence to: fengwang76@berkeley.edu

S1. Effective AC circuit model

S1. Effective AC circuit model

We use an effective AC RC circuit, shown in Figure 1c, to model the AC electrical transport in the TMDC heterostructure. C_1 and C_B are the geometric capacitances between the TMDC and the top and bottom gates in region 1, respectively, and C_2 is the geometric capacitance between the TMDC and the bottom gate in region 2. The geometric capacitances are defined by $C_i = \frac{\varepsilon_0 \varepsilon_r A_i}{d_i}$, where ε_r is the dielectric constant of the gate dielectric, and A_i and d_i denote the relevant capacitor area and separation. C_Q and R are the quantum capacitance and resistance of region 1, respectively. The ODRC signal measures the modulation induced optical contrast change in region 2, which can be understood as the optical response to an effective voltage change on region 2 (ΔV_2) due to the AC capacitive excitation in region 1 ($\Delta\tilde{V}$):

$$\Delta V_2 = \Delta\tilde{V}\left(1 - \frac{\frac{1}{i\omega C_1}}{\frac{1}{i\omega C_1} + \frac{1}{i\omega C_B + \frac{1}{\frac{1}{i\omega C_Q} + \frac{1}{i\omega C_2} + R}}}\right)\frac{\frac{1}{i\omega C_2}}{\frac{1}{i\omega C_Q} + R + \frac{1}{i\omega C_2}},$$

which can be simplified to:

$$\Delta V_2 = \Delta\tilde{V}\left(\frac{C_1}{C_1 + C_B}\right)\frac{\frac{1}{C_2}}{\frac{1}{(C_1 + C_B)} + \frac{1}{C_Q} + \frac{1}{C_2} + i\omega R}.$$

For simplicity, we define an effective capacitance as

$$\frac{1}{C_{eff}} = \frac{1}{(C_1 + C_B)} + \frac{1}{C_2} + \frac{1}{C_Q},$$

so

$$\Delta V_2 = \Delta\tilde{V}\left(\frac{C_1}{C_1 + C_B}\right)\frac{\frac{1}{C_2}}{\frac{1}{C_{eff}} + i\omega R}.$$

The effective voltage change leads to a total charge change $\Delta\tilde{Q}$ in region 2:

$$\Delta\tilde{Q} = \Delta V_2 C_2 = \Delta\tilde{V}\left(\frac{C_1}{C_1 + C_B}\right)\frac{1}{\frac{1}{C_{eff}} + i\omega R},$$

and corresponding change in hole density:

$$\Delta\tilde{n} = \frac{\Delta\tilde{Q}}{A_2 e} = \frac{1}{A_2 e}\Delta\tilde{V}\left(\frac{C_1}{C_1 + C_B}\right)\frac{1}{\frac{1}{C_{eff}} + i\omega R}$$

where e is the electron charge. The ODRC signal, ΔOC, is related to $\Delta\tilde{n}$ by the optical detection responsivity α, which describes the change in the optical absorption for a given change in doping:

$$\Delta OC = \alpha\Delta\tilde{n} = \frac{\alpha}{A_2 e}\Delta\tilde{V}\left(\frac{C_1}{C_1 + C_B}\right)\frac{1}{\frac{1}{C_{eff}} + i\omega R}.$$

The responsivity α is set to 1.4 x 10^{-12} cm^2, so that $\frac{1}{C_{eff}} = \frac{1}{(C_1+C_B)} + \frac{1}{C_2}$ at high doping, where the quantum capacitance is much larger than the geometry capacitances and has negligible contribution. This value of α is also consistent with the value determined by the doping-dependent optical absorption of region 2.